Gross Moist Stability Analysis: Assessment of Satellite-Based Products in the GMS Plane

KUNIAKI INOUE

NOAA/GFDL, Princeton, New Jersey

LARISSA E. BACK

University of Wisconsin–Madison, Madison, Wisconsin

(Manuscript received 25 July 2016, in final form 13 January 2017)

ABSTRACT

New diagnostic applications of the gross moist stability (GMS) are proposed with demonstrations using satellite-based data. The plane of the divergence of column moist static energy (MSE) against the divergence of column dry static energy (DSE), referred to as the GMS plane here, is utilized. In this plane, one can determine whether the convection is in the amplifying phase or in the decaying phase; if a data point lies below (above) a critical line in the GMS plane, the convection is in the amplifying (decaying) phase. The GMS plane behaves as a phase plane in which each convective life cycle can be viewed as an orbiting fluctuation around the critical line, and this property is robust even on the MJO time scale. This phase-plane behavior indicates that values of the GMS can qualitatively predict the subsequent convective evolution. This study demonstrates that GMS analyses possess two different aspects: time-dependent and quasi-time-independent aspects. Transitions of time-dependent GMS can be visualized in the GMS plane as an orbiting fluctuation around the quasi-time-independent GMS line. The time-dependent GMS must be interpreted differently from the quasi-time-independent one, and the latter is the GMS relevant to moisture-mode theories. The authors listed different calculations of the quasi-time-independent GMS: (i) as a regression slope from a scatterplot and (ii) as a climatological quantity, which is the ratio of climatological MSE divergence to climatological DSE divergence. It is revealed that the latter, climatological GMS, is less appropriate as a diagnostic tool. Geographic variations in the quasi-time-independent GMS are plotted.

1. Introduction

It is well known that tropical convection and column-integrated water vapor (also known as precipitable water) are closely related. Past work showed that there is a positive correlation between precipitable water and precipitation (e.g., Raymond 2000; Bretherton et al. 2004; Neelin et al. 2009; Masunaga 2012). This moisture–precipitation relationship plays a key role in an interaction between convection and associated large-scale circulations in the tropics; the ensemble of subgrid-scale convection alters large-scale circulations, and the large-scale circulations, in turn, change the local environment to be favorable or unfavorable for the convection via changing the local moisture condition. In this study, we present new diagnostic applications of a conceptual quantity called the gross moist stability (GMS) to investigate that interaction.

Column-integrated moist static energy (MSE) budgets are useful for investigating tropical convective disturbances. Temperature anomalies are small in the deep tropics owing to a large Rossby radius (e.g., Charney 1963; Bretherton and Smolarkiewicz 1989), which leads to a framework called the weak temperature gradient approximation (WTG; Sobel and Bretherton 2000; Sobel et al. 2001). This property of the tropics indicates that analyses of column MSE budgets approximately tell us about the processes associated with the growth and decay of precipitable water. And these analyses are most likely if not always accompanied by a quantity called the GMS.

The GMS, which represents the efficiency of the advective export of MSE by large-scale circulations associated with convection, was originally coined by Neelin and Held (1987) with a simple two-layer atmospheric

Corresponding author e-mail: Kuniaki Inoue, kuniaki.inoue@noaa.gov

DOI: 10.1175/JAS-D-16-0218.1

model. Two decades later, Fuchs and Raymond (2007) and Raymond et al. (2007) expanded this idea by defining a relevant quantity called the normalized GMS (NGMS) to include more general atmospheric structures. Since then, different authors have used slightly different definitions of the NGMS [see a review by Raymond et al. (2009)], but the philosophies behind them are the same: they all represent the amount of MSE (or moist entropy) exported per unit intensity of convection. In this study, the NGMS is simply called the GMS.

The GMS represents a feedback effect; when ignoring diabatic effects, negative GMS corresponds to a positive feedback in which moist regions become moister and dry regions become drier as a result of atmospheric motions (e.g., Sessions et al. 2010). Negative values of the GMS are associated with the intensification of convection via a positive feedback loop associated with atmospheric motions. Recent diagnostic studies showed that time-dependent GMS is a useful diagnostic tool to study the intensification of convection; for instance, they found that a reduction of the GMS is a precursor of the onset of deep strong convection in mesoscale convective disturbances (e.g., Masunaga and L'Ecuyer 2014; Inoue and Back 2015b). In this work, we further examine the relationship between GMS and convective growth and decay. We show that convective life cycles [both several-day cycles and the Madden–Julian oscillation (MJO)] can be represented in a phase plane of column MSE divergence versus column dry static energy (DSE) divergence.

Recently, the GMS has gained increasing attention because the idea is growing that the Madden–Julian oscillation is a moisture mode (e.g., Neelin and Yu 1994; Sobel et al. 2001; Sobel and Gildor 2003; Fuchs and Raymond 2002, 2005, 2007; Raymond and Fuchs 2007; Sugiyama 2009; Sobel and Maloney 2012, 2013; Adames and Kim 2016). According to this theory, a version of the GMS (often including some diabatic effects and hence called the effective GMS) plays a crucial role in the destabilization of the mode corresponding to the MJO.

However, the association between the GMS and moisture-mode stability in the real atmosphere is complex. Most of the moisture-mode theories are based on linear stability analysis. The method of the linear stability analysis consists of introducing sinusoidal disturbances on the "background" state to be examined and determining whether the background state demands the growth or decay of the introduced disturbances. Thus, what determines the stability of modes is its background state, and the GMS associated with the moisture-mode stability has to be "background GMS." However, background GMS can be estimated in a variety of different ways. The pioneering work by Yu et al. (1998) showed global maps of a version of background GMS. These authors, however, made strong assumptions about the structure of the vertical motion profile, which are likely not borne out in the real world (e.g., Back and Bretherton 2006). In this study, we clarify how to assess time-dependent and background components of the GMS separately using satellite data. The methodology can also be compared to other datasets like reanalysis and numerical model output.

The rest of this paper is structured as follows. This study is verification and extensions of the ideas proposed by Inoue and Back (2015b), which are briefly summarized in the next section. Section 3 presents the descriptions of the datasets and the choice of the spatial domains for the analyses. Using those datasets, we verify the proposed ideas in sections 4a and 4b. We also propose in section 4c a novel diagnostic framework in which convective life cycles are plotted in a phase plane of column MSE divergence versus column DSE divergence, which we refer to as the GMS plane analysis. This illustrates transient properties of the GMS throughout a convective life cycle. Furthermore, in section 4d, we examine the properties of quasi-time-independent "background GMS" and show geographic variability of this quantity. In section 4e, we briefly demonstrate the GMS plane analysis on the MJO time scale using field campaign data. A discussion about the GMS plane analysis and what circumstances it is relevant to are presented in section 5a. In section 5b, we discuss how to calculate the GMS relevant to moisture-mode instability and why the time-dependent version of the GMS does not represent the stability of a moisture mode. Section 6 concludes this study.

2. Summary of Inoue and Back (2015b)

Following Yanai et al. (1973), we start with the vertically integrated energy and moisture budget equations:

$$\frac{\partial\langle s\rangle}{\partial t} = -\nabla\cdot\langle s\mathbf{v}\rangle + \langle Q_R\rangle + LP + H \quad \text{and} \tag{1}$$

$$\frac{\partial\langle Lq\rangle}{\partial t} = -\nabla\cdot\langle Lq\mathbf{v}\rangle + LE - LP, \tag{2}$$

where $s \equiv c_pT + gz$ is DSE; c_pT is enthalpy; gz is geopotential; Q_R is radiative heating rate; L is the latent heat of vaporization; P is precipitation; H is surface sensible heat flux; q is water vapor mixing ratio; E is surface evaporation; the angle brackets represent a mass-weighted column integration from surface pressure to 100 hPa; and the other terms are in accordance

with meteorological conventions. We neglected the residual in these equations.

When considering a time scale longer than a diurnal cycle, the Eulerian tendency of column DSE is much smaller than that of precipitable water in the deep tropics. Thus, on such a time scale, adding Eqs. (1) and (2) approximately yields

$$\frac{\partial\langle Lq\rangle}{\partial t} \simeq -\nabla\cdot\langle h\mathbf{v}\rangle + \langle Q_R\rangle + S, \tag{3}$$

where $h \equiv s + Lq$ is MSE and $S \equiv LE + H$ is surface fluxes (generally H is negligible over the tropical oceans).

As claimed by past studies, there is a positive correlation[1] between precipitation and precipitable water. Thus, we have the following proportionality:

$$\frac{\partial P}{\partial t} \sim \frac{\partial\langle q\rangle}{\partial t}. \tag{4}$$

This relationship indicates that, when the RHS of Eq. (3) is positive (negative), the convection amplifies (decays). Although this seems to be an oversimplification, we will show it describes convective amplification and decay very well.

It must be cautioned here that the words ''amplification'' and ''decay'' of local convection in this study are used differently than the words ''destabilization'' and ''stabilization'' of linear modes, and thus those must not be confused with each other. The destabilization of linear modes means an increase in the amplitude of sinusoidal waves: positive anomalies become more positive, and negative anomalies become more negative. In contrast, the amplification of local convection simply means intensification of convection in the Eulerian frame; we cannot say the whole mode is destabilized simply because convection at one location amplifies.

Inoue and Back (2015b) did not examine Eq. (3) as it is, but they divided it by $\nabla\cdot\langle s\mathbf{v}\rangle$, which represents the intensity of convection (or convective heating), converting the MSE budget equation into a unitless efficiency equation:

$$\nabla\cdot\langle s\mathbf{v}\rangle^{-1}\frac{\partial\langle Lq\rangle}{\partial t} \simeq -(\Gamma - \Gamma_C), \tag{5}$$

where

$$\Gamma \equiv \frac{\nabla\cdot\langle h\mathbf{v}\rangle}{\nabla\cdot\langle s\mathbf{v}\rangle} \quad \text{and} \tag{6}$$

$$\Gamma_C \equiv \frac{D}{\nabla\cdot\langle s\mathbf{v}\rangle}, \tag{7}$$

In these equations $D \equiv \langle Q_R\rangle + S$ is the diabatic source,[2] Γ is the (normalized) GMS, and Γ_C is an analog of the GMS named the critical GMS by Inoue and Back (2015b), which represents the contribution of the diabatic source to column moistening. The difference $\Gamma - \Gamma_C$ is collectively called the drying efficiency because it represents the efficiency of the loss of water vapor due to convection. This drying efficiency may appear to be a version of the effective GMS (e.g., Su and Neelin 2002; Bretherton and Sobel 2002; Peters and Bretherton 2005; Sobel and Maloney 2012; Adames and Kim 2016) and is close to the effective GMS used by Hannah and Maloney (2014) and Sakaeda and Roundy (2016). However, the drying efficiency computed in this study must be interpreted as a different quantity from the effective GMS used in theoretical studies. Hence, we refer to it as the drying efficiency rather than the effective GMS. We clarify the distinction between them, together with the distinction between the GMS computed as a time-dependent quantity and the one used in theoretical studies, in section 5b.

Equation (5) has two benefits that Eq. (3) does not possess. First, because Eq. (5) is independent of a convective intensity, we can take composites of all convective events with different intensities. According to Eqs. (4) and (5), we can define two convective phases:

$$\Gamma - \Gamma_C < 0 \quad \text{and} \tag{8a}$$

$$\Gamma - \Gamma_C > 0; \tag{8b}$$

namely, the amplifying phase and the decaying phase, respectively. These relationships hold only when the denominator of the drying efficiency, $\nabla\cdot\langle s\mathbf{v}\rangle$, is positive. We generalize this condition to include the whole convective life cycle by utilizing the GMS plane in section 4c.

The second benefit, which we verify in section 4b, is that the critical GMS Γ_C turns out to be relatively constant. That simplifies the phases of Eqs. (8a) and (8b) into

$$\Gamma - \gamma < 0 \quad \text{and} \tag{9a}$$

$$\Gamma - \gamma > 0, \tag{9b}$$

[1] The actual relationship is in a nonlinear form (exponential or power law). This study is not sensitive to those details.

[2] In Inoue and Back (2015b), this was called the diabatic forcing. But the word ''forcing'' might be misleading, because radiative heating and surface fluxes are, to some extent, an intrinsic property of convection instead of external forcing. Thus, we simply call it the diabatic (MSE) source in this study.

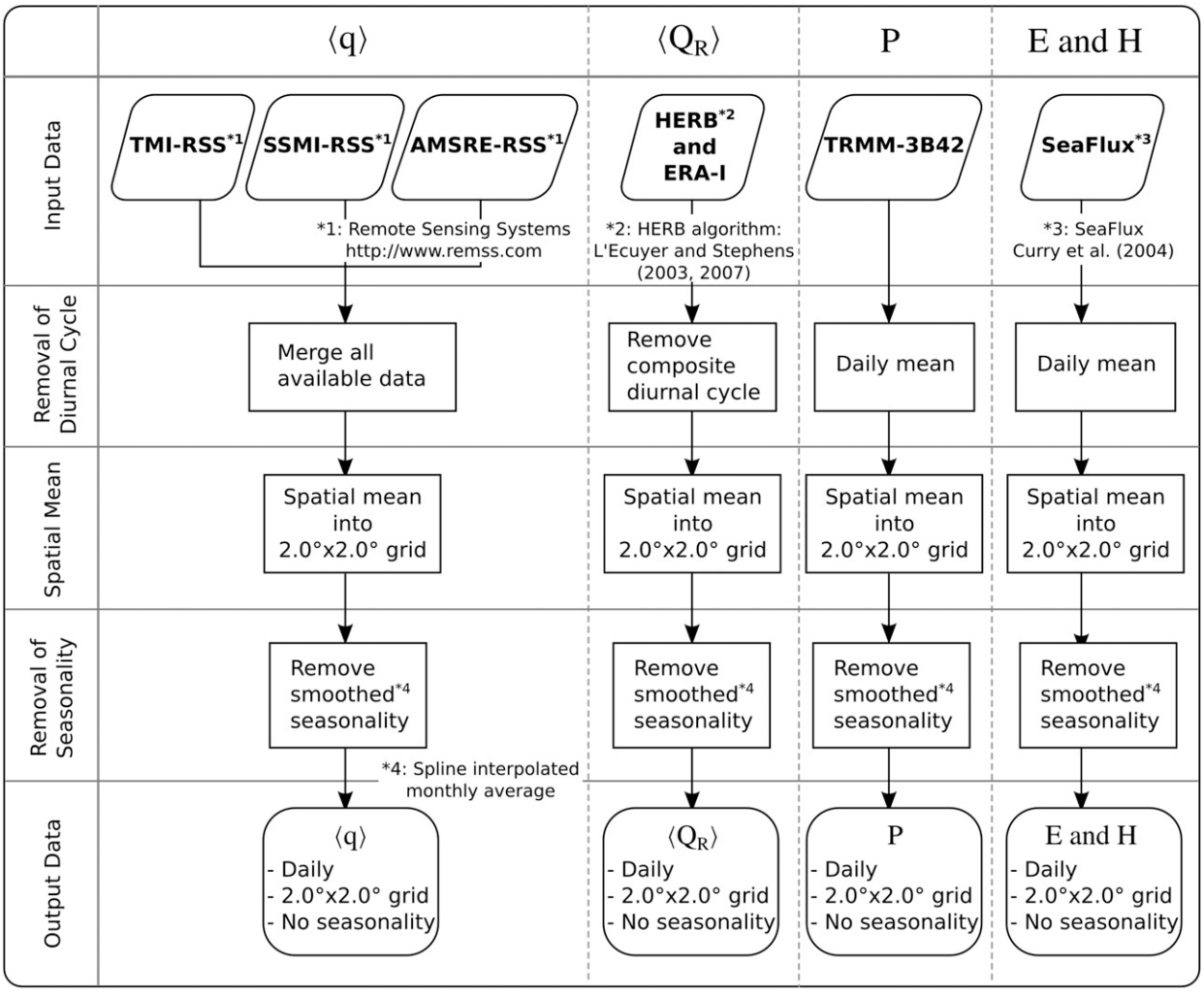

FIG. 1. Flowchart of the data procedures. See the text for details.

where γ is some constant that is explained in more detail in sections 4b and 4d. Those phases indicate that, when the GMS is smaller (bigger) than some critical constant, the convection amplifies (decays).

3. Data description

From satellite views, we can observe the RHSs of the following equations:

$$\nabla \cdot \langle s\mathbf{v} \rangle \simeq \langle Q_R \rangle + LP + H \quad \text{and} \tag{10}$$

$$\nabla \cdot \langle h\mathbf{v} \rangle \simeq \langle Q_R \rangle + S - \frac{\partial \langle Lq \rangle}{\partial t}. \tag{11}$$

In these equations, the column DSE tendency, which is much smaller than the other terms (e.g., Inoue and Back 2015b), was neglected. By using satellite-based data, we can compute the GMS Γ, critical GMS Γ_C, and drying efficiency $\Gamma - \Gamma_C$ as follows:

$$\Gamma = \frac{\langle Q_R \rangle + S - \partial \langle Lq \rangle / \partial t}{\langle Q_R \rangle + LP + H}, \tag{12}$$

$$\Gamma_C = \frac{\langle Q_R \rangle + S}{\langle Q_R \rangle + LP + H}, \quad \text{and} \tag{13}$$

$$\Gamma - \Gamma_C = -\frac{\partial \langle Lq \rangle / \partial t}{\langle Q_R \rangle + LP + H}. \tag{14}$$

The values of $\nabla \cdot \langle s\mathbf{v} \rangle$ and $\nabla \cdot \langle h\mathbf{v} \rangle$ were computed as the residual of Eqs. (10) and (11). The procedures of the data treatments are summarized in Fig. 1, which consist of three steps: removal of diurnal cycles, spatial average, and removal of seasonality.

Diurnal cycles need to be removed from all the budget terms; otherwise, we cannot neglect the column DSE

tendency (e.g., Inoue and Back 2015b). The methodologies of diurnal-cycle removal depend on the datasets, which are described more specifically in the next subsection. The spatial grid size was changed into 2° × 2° by taking a spatial average in order to minimize sampling errors. Furthermore, we removed seasonality (or variability with periodicity longer than a month) from all the terms in order to minimize the effects of a seasonal convergence-zone shift. More detailed descriptions are presented in the following.

a. Data source and procedure

1) PRECIPITABLE WATER

The precipitable water retrievals used in this study are derived from the TRMM Microwave Imager (TMI), a series of Special Sensor Microwave Imagers (SSM/I F13, F14, F15, and F16) on Defense Meteorological Satellite Program (DMSP) satellites, and Advanced Microwave Scanning Radiometer for Earth Observing System (AMSR-E) on *Aqua*. The datasets are provided by Remote Sensing Systems (RSS; Wentz et al. 2012, 2014, 2015).

For removing the diurnal cycles, we took an ensemble average of all the precipitable water data from the different satellite sensors listed above. Since each sensor flies over a given place at different local time, and diurnal cycles of precipitable water are not so large (not shown here), we expect this method minimizes the contamination due to the diurnal cycles. This method also allows us to obtain daily precipitable water data over the entire tropical ocean so that we can compute a snapshot of precipitable water tendency with center differencing over two days at any time and place over the whole tropical ocean. The precipitable water tendency data (0.25° × 0.25° grids) were spatially averaged into 2° × 2° grids.

Next, we removed variability with periodicity longer than 1 month as follows. First, we took a monthly average of the anomalies of the data to construct a monthly anomalous time series. Then, by applying a spline interpolation to that monthly time series, we constructed a smoothed seasonality time series at each day, which was subtracted from the daily data. By this method, we expect the effects associated with the seasonal ITCZ shift are minimized. This methodology also removed most of the MJO variability from the dataset. Analyses of MJO time-scale variability were done separately using different data, which are briefly shown in section 4e.

2) RADIATIVE HEATING

The radiative heating estimates based on the TMI are derived with the algorithm called the Hydrologic Cycle and Earth's Radiation Budget (HERB: L'Ecuyer and Stephens 2003, 2007). The raw data used here, which exist only over the TMI swath, are instantaneous, 0.5° × 0.5° averages. For a vertical integration, we used the geopotential from the European Centre for Medium-Range Weather Forecasts interim reanalysis (ERA-Interim; Dee et al. 2011), which are the only nonsatellite data we used in this study. The grid size of the geopotential (~0.7° × 0.7°) was changed into the same one as the radiative heating with a linear interpolation.

The diurnal cycles of the column radiative heating were computed based on the property of a sun-asynchronous TRMM orbit. We constructed the climatological diurnal cycles at each place by sorting the data array into 6-hourly bins and taking an average within those bins. Those constructed diurnal cycles were removed from the raw data at each place. The column radiative heating data with diurnal cycles removed were spatially averaged into 2° × 2° grids. Finally, the seasonality computed with a spline interpolation was removed in the same way as for the precipitable water.

3) PRECIPITATION

For precipitation, we used version 7 of the daily TRMM Multisatellite Precipitation Analysis (TMPA) known as the 3B42 product (Huffman et al. 2007, 2010). The daily raw data given in 0.25° × 0.25° grids were spatially averaged into 2° × 2° grids, and a smoothed seasonality was removed in the same way as described above.

4) SURFACE FLUXES

The surface flux data, including surface sensible heat flux and surface evaporation, were obtained from SeaFlux (Curry et al. 2004), which is a dataset relying almost exclusively on satellite observations. The 6-hourly, 0.25° × 0.25° raw data were regridded into daily, 2° × 2° grids with a daily and spatial average. Similar to the other variables, a spline-interpolated seasonality was removed.

b. Spatial domain for analysis

For the analyses, we chose four spatial domains, depicted in Fig. 2, from the basins of the Indian Ocean (IO), the western Pacific Ocean (WP), the central–eastern Pacific Ocean (EP), and the Atlantic Ocean (AO). The regions surrounded by the polygons in Fig. 2 are analyzed separately in the following sections.

First, we set the rectangular boxes defined by 5°S–5°N, 60°–90°E; 5°S–5°N, 150°–180°E; 0°–15°N, 190°–250°E; and 0°–15°N, 300–360°E for IO, WP, EP, and AO, respectively. And the regions with the mean precipitation (from 2000 to 2007) greater than 5 mm day^{-1} were

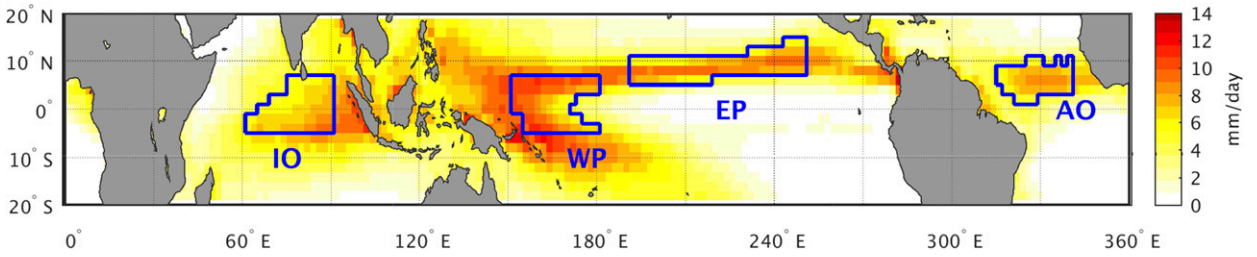

FIG. 2. Spatial domains for analyses and mean precipitation from 2000 to 2007. We investigated the regions surrounded by the polygons in the four oceanic basins: the Indian Ocean (IO), the western Pacific Ocean (WP), the central–eastern Pacific Ocean (EP), and the Atlantic Ocean (AO).

chosen for the analyses. Over these regions, the quantities of interest, which are discussed in section 4d, are fairly homogeneous.

There are 70, 74, 88, and 47 grids surrounded by the boundaries for IO, WP, EP, and AO, respectively. In each domain, we concatenated all 8-yr-long time series from 2000 to 2007 at different grid points into a long data array. This means each data array has a number of data points equal to, at least, the number of grids $\times$ 8 yr $\times$ 365 day $\times$ TMI swath coverage rate ($\sim$70%).

4. Results

a. Convective amplification and decay

As in Inoue and Back (2015b), we first verify the idea of the convective amplification and decay phases defined by Eqs. (8a) and (8b), respectively. In doing so, we plotted in Fig. 3a changes of precipitation over 2 days, in Fig. 3b probabilities of increase in precipitation, and in Fig. 3c precipitation, as a function of the drying efficiency $\Gamma - \Gamma_C$. Because the phases of Eqs. (8a) and (8b) hold only when convection is active or $\nabla \cdot \langle s\mathbf{v} \rangle$ is positive, we removed all the data points with $\nabla \cdot \langle s\mathbf{v} \rangle$ less than 50 W m^{-2} in order to exclude convectively inactive times and to avoid division by zero. Furthermore, 2.5% outliers from the left and right tails of the PDF of $\Gamma - \Gamma_C$ were also removed to avoid biases due to very large and small values of $\Gamma - \Gamma_C$. Those threshold values are arbitrary, and the results shown are insensitive to them. In section 4c, we generalize this condition and investigate the whole convective life cycle.

Figure 3a, which shows precipitation changes as a function of $\Gamma - \Gamma_C$, was made as follows. First, we sorted the data array of precipitation changes, computed with a centered difference over 2 days, in accordance with the order of $\Gamma - \Gamma_C$, and all the data points corresponding to $\nabla \cdot \langle s\mathbf{v} \rangle$ less than 50 W m^{-2} and 2.5% outliers of $\Gamma - \Gamma_C$ were removed. That sorted data array was averaged within five-percentile bins of $\Gamma - \Gamma_C$ to render Fig. 3a. Figure 3b, which illustrates probabilities of increase in precipitation against $\Gamma - \Gamma_C$, was made similarly. We computed the ratio of the number of events with positive precipitation changes to the total event number within the five-percentile bins of $\Gamma - \Gamma_C$.

Both Figs. 3a and 3b strongly support the hypothesis of the convective amplification and decay phases. When the drying efficiency $\Gamma - \Gamma_C$ is negative (positive), the

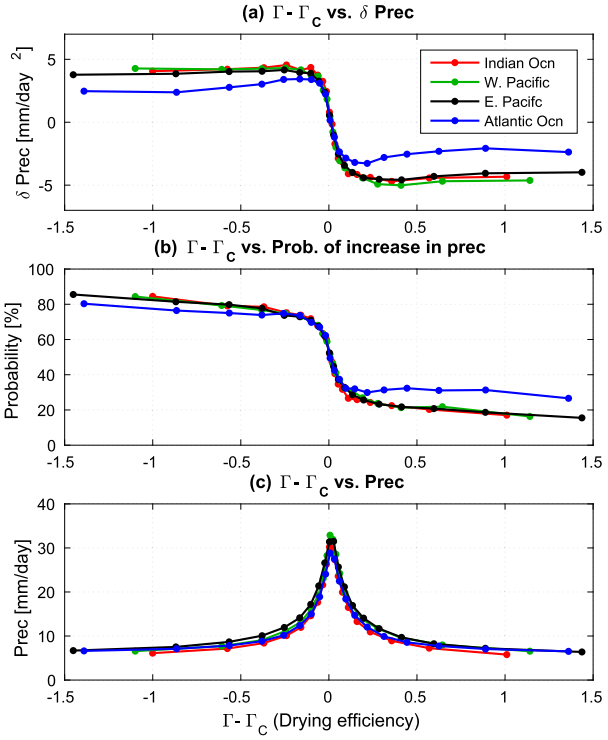

FIG. 3. (a) Binned precipitation changes as a function of the drying efficiency $\Gamma - \Gamma_C$, averaged in 5-percentile bins of $\Gamma - \Gamma_C$. Temporal precipitation changes δPres were computed with a centered difference over 2 days. (b) Probabilities of increase in precipitation as a function of $\Gamma - \Gamma_C$, computed in the same bins as (a). (c) Binned precipitation as a function of $\Gamma - \Gamma_C$, computed in the same way as above. Each analysis was conducted within the domains depicted in Fig. 2: IO (red), WP (green), EP (black), and AO (blue).

precipitation amplifies (decays) in the next day, that is, positive (negative) precipitation changes at high probability (~80%), and when $\Gamma - \Gamma_C$ changes its sign, the phase abruptly switches. This pattern is robust among all the oceanic basins, as shown with the lines in different colors.

When considering significant scatter in plots of P versus $\langle q \rangle$ in general, the assumption of the positive correlation between P and $\langle q \rangle$ in Eq. (4) seems to be an oversimplification. In spite of the seemingly oversimplified assumption, the amplifying and decaying phases defined by $\Gamma - \Gamma_C$ were far more robust than we expected. This significant predictability is not obvious from scatterplots of P versus $\langle q \rangle$ in general.

Figure 3c illustrates precipitation as a function of $\Gamma - \Gamma_C$, rendered with the same binning method as the others. In the amplifying phase (i.e., $\Gamma - \Gamma_C < 0$), the precipitation increases as $\Gamma - \Gamma_C$ becomes less negative and reaches the maximum when $\Gamma - \Gamma_C$ is zero, that is, when Γ is equal to Γ_C; in the decaying phase (i.e., $\Gamma - \Gamma_C > 0$), the precipitation decreases with increase in $\Gamma - \Gamma_C$. The occurrence of the maximum precipitation at $\Gamma - \Gamma_C$ (or $\Gamma - \Gamma_C = 0$) is rooted in the fact that the local maximum of precipitable water and precipitation happens when $\partial \langle q \rangle / \partial t \simeq 0$. The precipitation minimum also happens when $\Gamma = \Gamma_C$, but convectively inactive times were removed through the procedures described above.

In the next subsection, we show that Γ_C can be approximated as a constant in the satellite data used. This indicates that the phase of convection is determined by the criticality of the GMS (i.e., whether Γ is greater or less than some critical constant). This is why we refer to Γ_C as the critical GMS.

b. Constancy of critical GMS

Figure 4 shows scatterplots for the diabatic source ($D \equiv \langle Q_R \rangle + S$) and divergence of column MSE ($+\nabla \cdot \langle h\mathbf{v} \rangle$) as a function of divergence of column DSE ($+\nabla \cdot \langle s\mathbf{v} \rangle$) over the four oceanic basins. The color shade represents the base-10 logarithm of the number of occurrences within $12.5\,\mathrm{W\,m^{-2}} \times 25.0\,\mathrm{W\,m^{-2}}$ grids of D (or $\nabla \cdot \langle h\mathbf{v} \rangle$) and $\nabla \cdot \langle s\mathbf{v} \rangle$. The black dashed line in each panel was computed with regression through the origin, and the gray line was computed with the binning average within $\nabla \cdot \langle s\mathbf{v} \rangle$ bins that were $200\,\mathrm{W\,m^{-2}}$ wide.

It can be seen in the left column of Fig. 4 that the scatter of D is concentrated along the regression line through the origin, and this pattern is similar among all the oceanic basins with slightly varying regression slopes. This linear trend of D appears to be robust, especially when compared with the scatter of $\nabla \cdot \langle h\mathbf{v} \rangle$ in the right column. Thus, we can approximate D as

$$D \simeq \gamma \nabla \cdot \langle s\mathbf{v} \rangle . \tag{15}$$

Strictly speaking, γ is not a constant but slightly varies depending on the value of $\nabla \cdot \langle s\mathbf{v} \rangle$, as depicted in the gray binned lines. But the regression lines capture well the overall trend of the scatter of D. Therefore, as proposed in section 2, we can approximate the critical GMS [Eq. (7)] to be γ, which is a constant relevant to the characteristic GMS defined by Inoue and Back (2015b) that is discussed in section 4d.

Now we can replace Γ_C in the drying efficiency $\Gamma - \Gamma_C$ with γ and define the amplifying and decaying phases in terms of $\Gamma - \gamma$ as Eqs. (9a) and (9b), respectively: Negative (positive) $\Gamma - \gamma$ corresponds to the amplifying (decaying) phase. Figure 5 verifies this idea, which was made in the same way as Fig. 3, but as a function of $\Gamma - \gamma$ instead of $\Gamma - \Gamma_C$. This figure illustrates that $\Gamma - \gamma$ works well to describe the convective amplification and decay phases among all the oceanic basins. Thus, we can claim that convection will most likely amplify (decay) when Γ is less (greater) than γ, and the local maximum happens at $\Gamma = \gamma$. This means that, if the value of γ is given, the GMS is telling us if the convection is amplifying or decaying.

As discussed in sections 2 and 4a, the phase relationships in terms of $\Gamma - \gamma$ hold only when $\nabla \cdot \langle s\mathbf{v} \rangle$ is positive. Now we generalize this condition to include the whole convective life cycle in the next subsection. This can be done by utilizing the linear trend in Eq. (15) and a diagnostic framework, which we refer to as the GMS plane.

c. GMS plane

By assuming the positive correlation between P and $\langle q \rangle$ in Eq. (4) and the linear trend of D in Eq. (15), we can derive a simple model:

$$\frac{\partial P}{\partial t} \sim \frac{\partial \langle Lq \rangle}{\partial t} \simeq -\nabla \cdot \langle h\mathbf{v} \rangle + \gamma \nabla \cdot \langle s\mathbf{v} \rangle . \tag{16}$$

This model is a generalization of the amplifying and decaying phases in Eqs. (9a) and (9b), respectively; when $\nabla \cdot \langle s\mathbf{v} \rangle$ is positive, we can divide this by $\nabla \cdot \langle s\mathbf{v} \rangle$ and yield the same relationships as Eqs. (9a) and (9b).

We bear out the validity of this simple model in Fig. 6, in which probabilities of increase in precipitation are plotted in the plane of $\nabla \cdot \langle h\mathbf{v} \rangle$ versus $\nabla \cdot \langle s\mathbf{v} \rangle$ that we call the GMS plane.[3] In this plane, the tangent of a phase angle corresponds to the GMS. The probabilities were

[3] Utilization of the GMS plane is not a new concept. For instance, some past studies analyzed scatterplots in the GMS plane (e.g., Raymond and Fuchs 2009; Benedict et al. 2014).

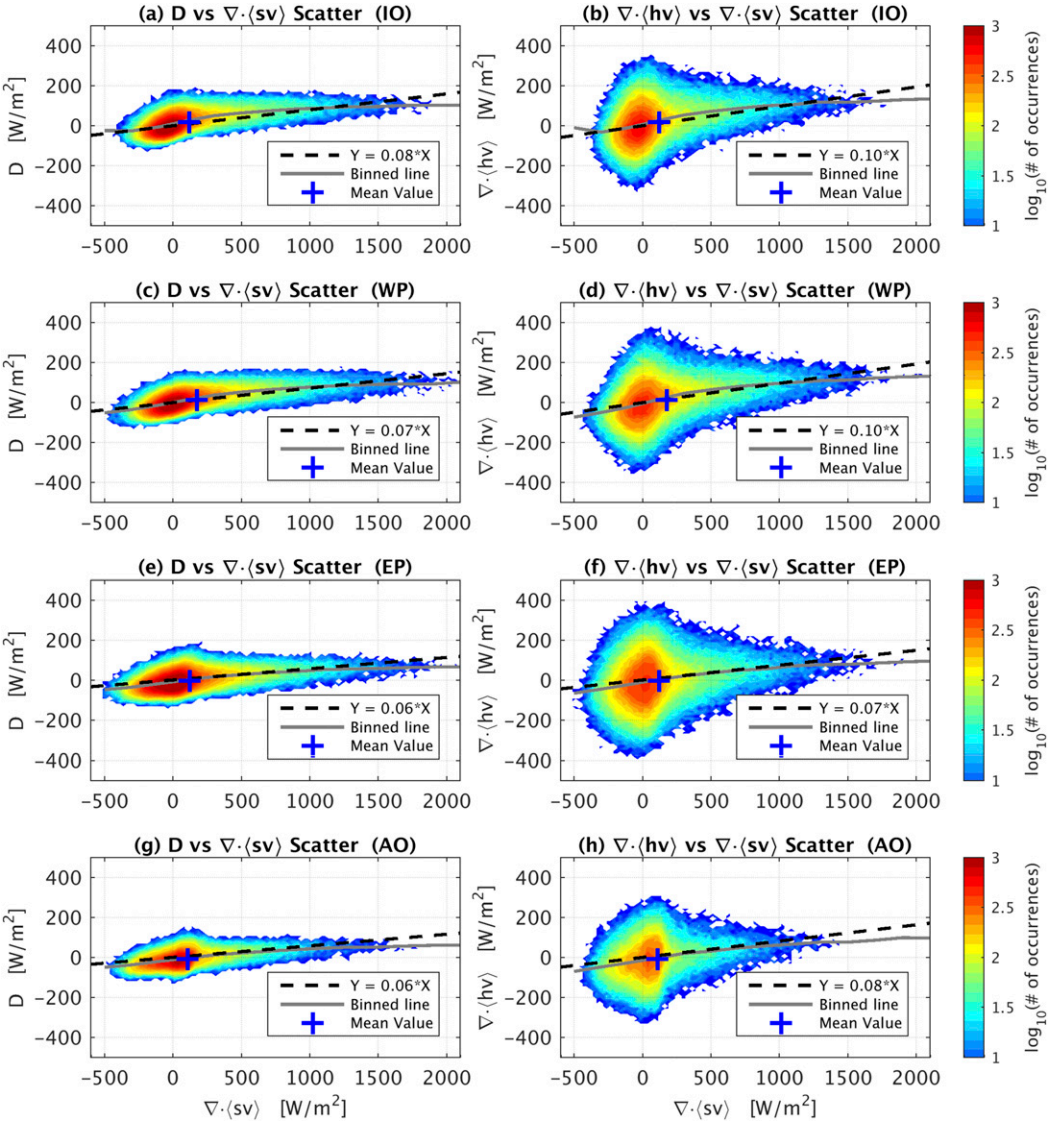

FIG. 4. (left) Scatterplots of diabatic source ($D \equiv \langle Q_R \rangle + S$) against divergence of column DSE ($+\nabla \cdot \langle s\mathbf{v} \rangle$) over the four oceanic basin regions: (a) IO, (c) WP, (e) EP, and (g) AO. (right) As in (left), but for divergence of column MSE ($+\nabla \cdot \langle h\mathbf{v} \rangle$). In each panel, the black dashed line was computed with the regression through the origin, and the gray line was computed with the binning average. The blue cross mark indicates the mean value.

computed similarly to Fig. 3, but now within 2D bins instead of 1D bins. We computed the ratio of the number of events with positive precipitation changes over 2 days to the total event number within $\nabla \cdot \langle h\mathbf{v} \rangle$ and $\nabla \cdot \langle s\mathbf{v} \rangle$ bins of $50\,\mathrm{W\,m^{-2}} \times 50\,\mathrm{W\,m^{-2}}$. The regression lines through the origin and the binned lines are identical to those in the left column of Fig. 4. The slopes of the regression lines correspond to γ, which is the approximated critical GMS Γ_C.

It is clear in this figure that the grids below (above) the critical line (i.e., the regression line) exhibit high (low) probabilities of convective amplification, and there is an abrupt transition near the critical line. This figure strongly supports the validity of the model in Eq. (16); the grids below (above) the critical line correspond to positive (negative) RHS of Eq. (16) and thus to the amplification (decay) of convection. Figure 6 is a generalized version of Fig. 3b.

This GMS plane is useful particularly because it acts like a phase plane. If a data point lies below the critical line, the convection will most likely intensify in the next day; thus, the data point will move toward the right in the GMS plane; in contrast, a data point above the critical line will move toward the left. Furthermore, we

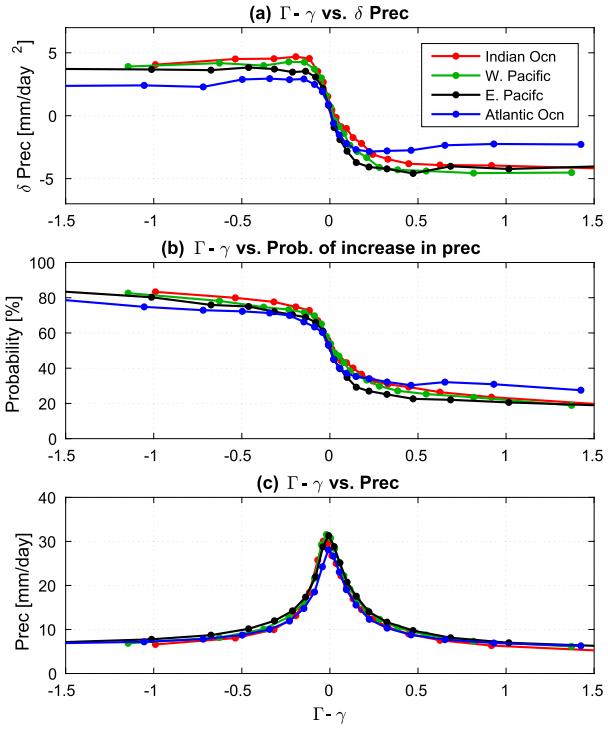

FIG. 5. As in Fig. 3, but the critical GMS Γ_C was replaced with the slopes of the regression lines γ in Figs. 4a,c,e,g.

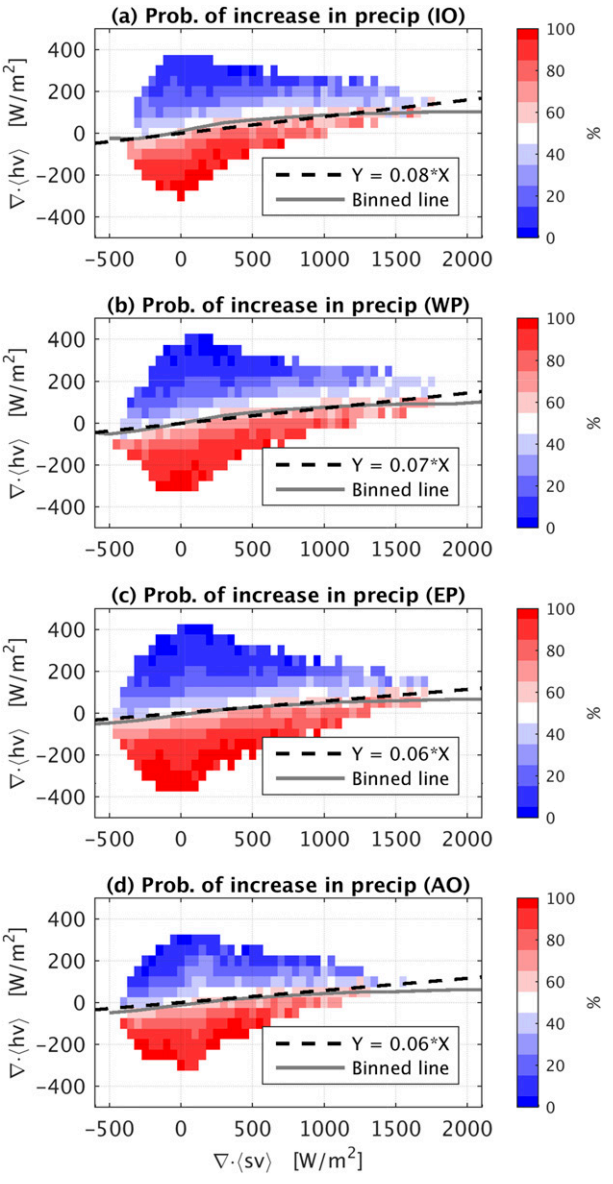

FIG. 6. Probabilities of increase in precipitation within grids of $\nabla \cdot \langle h\mathbf{v} \rangle$ and $\nabla \cdot \langle s\mathbf{v} \rangle$ over the four oceanic basins: (a) IO, (b) WP, (c) EP, and (d) AO. The probabilities were calculated within $50\,\mathrm{W\,m^{-2}} \times 50\,\mathrm{W\,m^{-2}}$ grids. The black dashed lines and the gray lines are identical to those in Figs. 4a,c,e,g.

know that precipitation reaches the maximum on the critical line (i.e., $\Gamma = \gamma$) from Fig. 5c. Thus, we expect that convective life cycles in the GMS plane look like orbiting fluctuations around the critical line. This idea is illustrated in Fig. 7, which shows the mean values of temporal changes of $\nabla \cdot \langle h\mathbf{v} \rangle$ and $\nabla \cdot \langle s\mathbf{v} \rangle$ as arrows at each grid in the GMS plane. The mean values were computed within bins of $100\,\mathrm{W\,m^{-2}} \times 100\,\mathrm{W\,m^{-2}}$. This figure illustrates that the GMS plane is a phase plane in which each convective life cycle tends to orbit around the critical GMS line. It should be noted that this phase plane behavior has been already claimed by Masunaga and L'Ecuyer (2014) and Inoue and Back (2015a), though not illustrated in this way.

Figure 7 is an alternative depiction of a GMS transition to plotting a time series of it. In general, computation of the GMS becomes troublesome when its denominator is small. Depicting a GMS transition as a phase transition in the GMS plane can avoid the computational problem of the GMS; thus, we can apply this methodology to the whole convective life cycle.

Since the behaviors illustrated in Figs. 6 and 7 are robust among all the oceanic basins with slightly varying regression slopes, we plotted in Fig. 8 those for the whole oceanic regions where the mean precipitation is greater than $5\,\mathrm{mm\,day^{-1}}$. The gray dashed and dotted lines in it represent the range of the geographic variability of a regression slope γ. This figure summarizes important aspects of the GMS: when considering $\nabla \cdot \langle s\mathbf{v} \rangle > 0$ and $\nabla \cdot \langle s\mathbf{v} \rangle < 0$ cases separately, values of the GMS (i.e., phase position in the GMS plane) have a capability to predict the subsequent convective evolution in a qualitative manner, and that law is quite universal throughout the whole tropical ocean. In the next subsection, we discuss the geographic variability of a

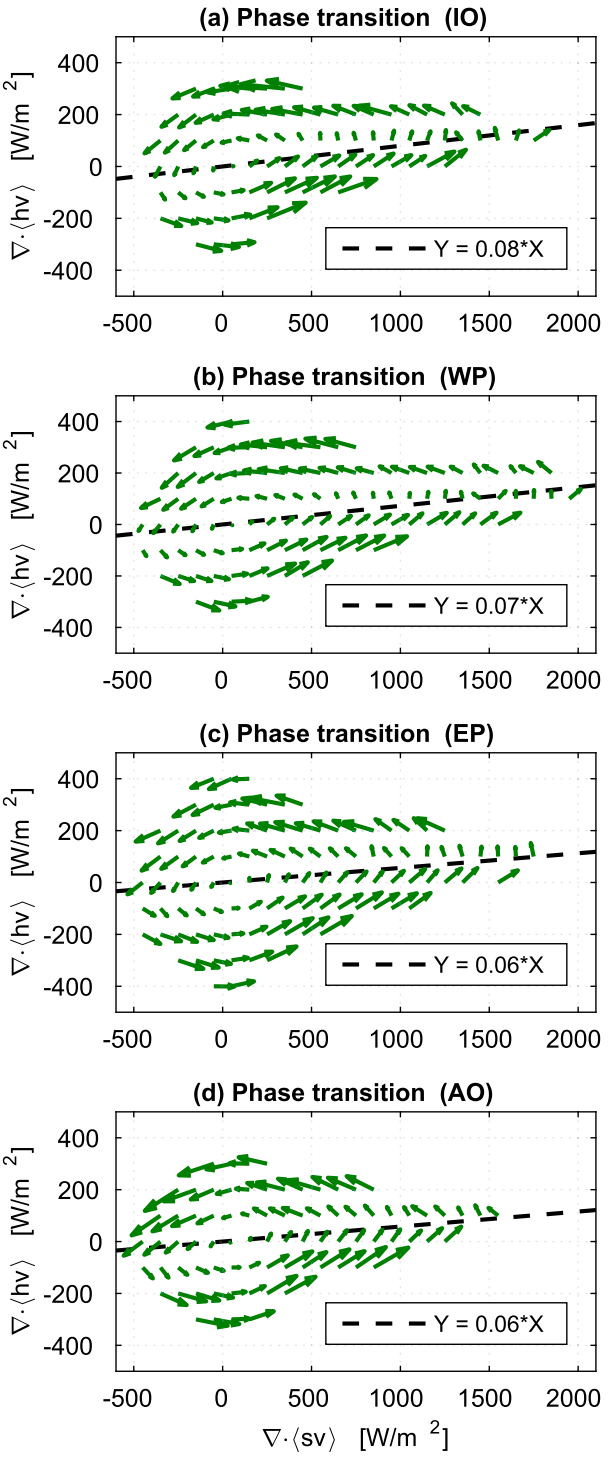

FIG. 7. Mean values of temporal changes of $\nabla \cdot \langle h\mathbf{v} \rangle$ and $\nabla \cdot \langle s\mathbf{v} \rangle$ (with a centered difference) at each grid in the GMS plane, represented by vector arrows, over the four domains: (a) IO, (b) WP, (c) EP, and (d) AO. The mean values were calculated within $100\,\mathrm{W\,m^{-2}} \times 100\,\mathrm{W\,m^{-2}}$ grids. The dashed lines are identical to those in Figs. 4a,c,e,g and Fig. 6.

regression slope γ, which is relevant to the characteristic GMS defined by Inoue and Back (2015b).

d. Characteristic GMS

So far, we have discussed a time-dependent aspect of the GMS. Now let us discuss the quasi-time-independent "background GMS," which we refer to as the characteristic GMS. In the following discussion, we clarify how to calculate a meaningful value of the background GMS.

In the previous sections, we introduced the critical GMS γ, calculated as a slope of a regression line through the origin, which represents a feedback between diabatic sources (column radiation and surface fluxes) and convection. And we showed that γ corresponds to a value of the GMS at the convective maximum $\Gamma_{\max}$. In addition to those, Inoue and Back (2015b) listed three different calculations of the background GMS as follows:

1) GMS calculated from a scatterplot of anomalous $\nabla \cdot \langle h\mathbf{v} \rangle$ against $\nabla \cdot \langle s\mathbf{v} \rangle$:

$$\tilde{\Gamma}' \equiv \frac{\overline{\nabla \cdot \langle h\mathbf{v} \rangle' \times \nabla \cdot \langle s\mathbf{v} \rangle'}}{\overline{\nabla \cdot \langle s\mathbf{v} \rangle'^2}}, \tag{17}$$

2) GMS calculated from a scatterplot of nonanomalous $\nabla \cdot \langle h\mathbf{v} \rangle$ against $\nabla \cdot \langle s\mathbf{v} \rangle$:

$$\tilde{\Gamma} \equiv \frac{\overline{\nabla \cdot \langle h\mathbf{v} \rangle \times \nabla \cdot \langle s\mathbf{v} \rangle}}{\overline{\nabla \cdot \langle s\mathbf{v} \rangle}^2}, \tag{18}$$

and

3) Climatological GMS:

$$\overline{\Gamma} \equiv \frac{\overline{\nabla \cdot \langle h\mathbf{v} \rangle}}{\overline{\nabla \cdot \langle s\mathbf{v} \rangle}}, \tag{19}$$

where the bar represents a time average and the prime represents departure from the time average. Thus, in total, we have five different ways of calculating the background GMS (γ, $\Gamma_{\max}$, $\tilde{\Gamma}'$, $\tilde{\Gamma}$, and $\overline{\Gamma}$), and Inoue and Back (2015b) claimed that all of them are close to each other so that they can be used interchangeably. They are collectively called the characteristic GMS. In the discussion below, we show that all versions of the characteristic GMS are close to each other over the whole tropical ocean, except for the climatological GMS $\overline{\Gamma}$, which is so sensitive to data errors that it should not be used as a diagnostic tool.

Figure 9 shows the geographic variability of the critical GMS γ (Fig. 9a), the anomalous characteristic GMS $\tilde{\Gamma}'$ (Fig. 9b), the nonanomalous characteristic GMS $\tilde{\Gamma}$

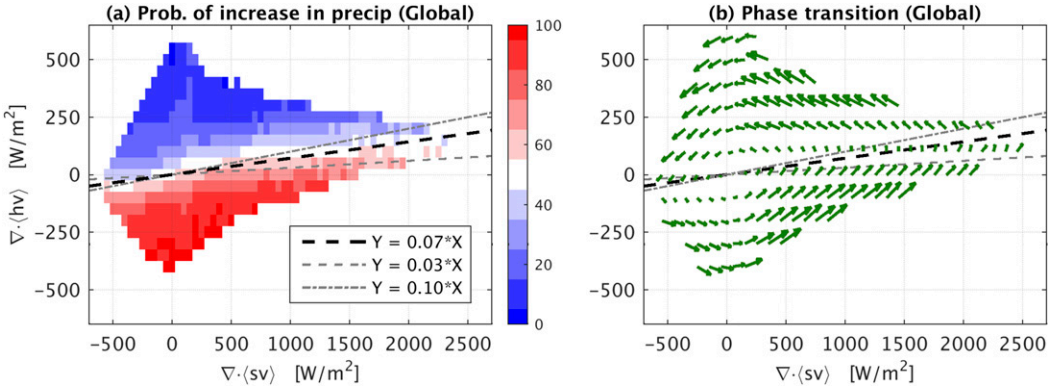

FIG. 8. (a) As in Fig. 6, but for the whole tropical convergence zone with the mean precipitation greater than 5 mm day^{-1} (the colored regions in Fig. 9). (b) As in Fig. 7, but for the whole tropical convergence zone. The slope of the black dashed line was computed similarly to that in Figs. 6 and 7, and the two gray lines represent the geographic variability of the critical GMS.

(Fig. 9c), and the climatological GMS $\overline{\Gamma}$ (Fig. 9d) over the oceanic regions where the mean precipitation is greater than 5 mm day^{-1}. The first three panels (Figs. 9a–c) exhibit similar geographic patterns; the values are slightly higher in the Indian and the western Pacific Oceans than in the central–eastern Pacific and the Atlantic Oceans. The correlations of the spatial pattern of Fig. 9a with Figs. 9b and 9c are 0.848 and 0.737, respectively. It should be noted that the color scales in Figs. 9b and 9c are shifted by 0.01 compared with that in Fig. 9a. That small departure is due to nonzero covariance between $\partial\langle q\rangle/\partial t$ and $\nabla\cdot\langle s\mathbf{v}\rangle$, owing to slight lags between P and $\langle q\rangle$ [see section 5 in Inoue and Back (2015b)].

The geographic patterns shown are, to some extent, consistent with the geographic variability of vertical velocity profiles. In general, shapes of vertical velocity profile are top-heavier (associated with greater GMS) in the Indian and the western Pacific Oceans with weak SST gradient and bottom-heavier (associated with smaller GMS) in the central–eastern Pacific and the Atlantic Oceans with strong SST gradient (e.g., Back and Bretherton 2006; Sobel and Neelin 2006; Back and Bretherton 2009a,b; Back et al. 2017). But it should be noted that the definitions of the characteristic GMS used here include both the horizontal and vertical components of the GMS, and thus their values cannot be determined solely by vertical velocity profiles. It would be interesting to investigate further the mechanisms that control the geographic patterns of the characteristic GMS.

Although the values of the three characteristic GMSs, γ, $\tilde{\Gamma}'$, and $\tilde{\Gamma}$, are consistent with each other, the climatological GMS $\overline{\Gamma}$ exhibits a quite different geographic pattern as depicted in Fig. 9d. It shows that $\overline{\Gamma}$ is negative in the eastern Pacific and the Atlantic Oceans, and the color scale is far different from those in the other panels. We claim that this significant discrepancy is due to the sensitivity of this metric to data errors. In Fig. 4, the mean values of $(\nabla\cdot\langle h\mathbf{v}\rangle, \nabla\cdot\langle s\mathbf{v}\rangle)$ are plotted with the blue cross marks. Their values are (19.3 W m^{-2}, 118.0 W m^{-2}), (15.3 W m^{-2}, 174.9 W m^{-2}), (−2.1 W m^{-2}, 120.9 W m^{-2}), and (−5.9 W m^{-2}, 107.1 W m^{-2}), respectively, for IO, WP, EP, and AO. One can notice that the numerator of $\overline{\Gamma}$, $\overline{\nabla\cdot\langle h\mathbf{v}\rangle}$, is a tiny number especially in EP and AO. Thus, even a few watts per square meter of its errors can cause crucial errors in $\overline{\Gamma}$ with a sign flip. Therefore, we conclude that the metric of the climatological GMS $\overline{\Gamma}$ is so sensitive to data errors that it should not be used as a diagnostic tool, especially with observational data involving nonnegligible biases. Recently, the GMS was used as a diagnostic tool for an intermodel comparison (e.g., Benedict et al. 2014; Hannah and Maloney 2014; Maloney et al. 2014). Because of the issues with the climatological GMS, it would be useful to use the versions of the characteristic GMS calculated from a scatterplot for this type of analysis in the future.

e. GMS transitions during DYNAMO

Last, we briefly show the GMS transitions on the MJO time scale. In doing so, we plotted in the GMS plane the transitions of different MJO events during the DYNAMO field campaign. We used version 3a of the Colorado State University quality-controlled observations from the DYNAMO field campaign (Johnson and Ciesielski 2013; Ciesielski et al. 2014a,b; Johnson et al. 2015). All the variables plotted are averages over the northern sounding array and are also 10-day running averages.

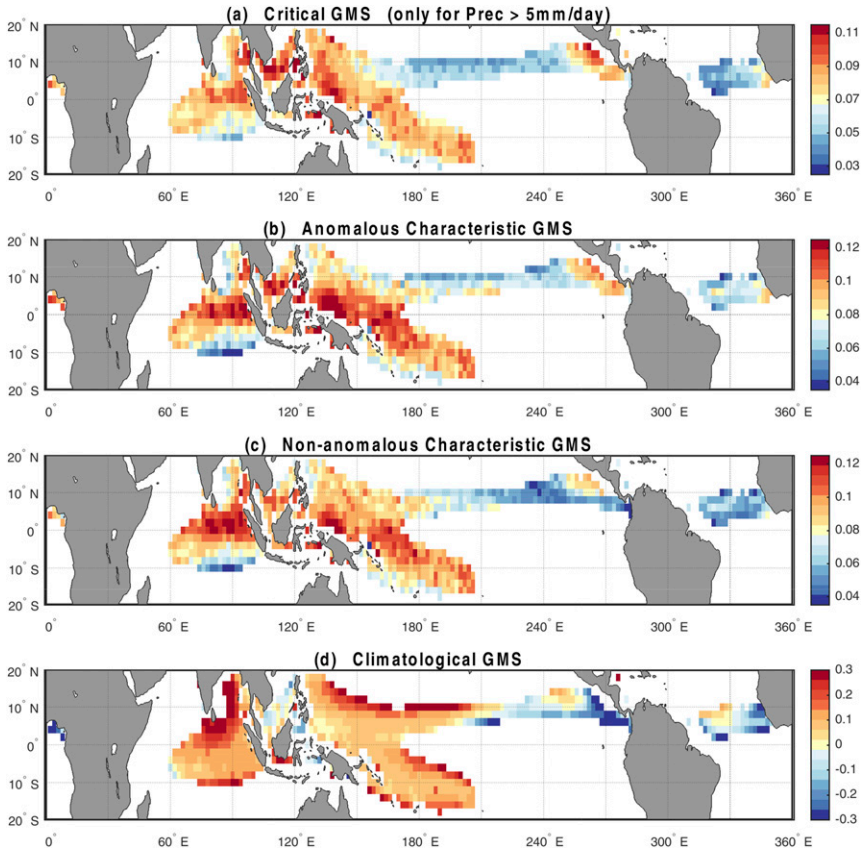

FIG. 9. (a) Map of critical GMS [γ in Eq. (15)] over the oceanic regions with the mean precipitation greater than 5 mm day^{-1}. (b) Map of anomalous characteristic GMS [$\tilde{\Gamma}'$ in Eq. (17)]. (c) Map of nonanomalous characteristic GMS [$\tilde{\Gamma}$ in Eq. (18)]. (d) Map of climatological GMS [$\overline{\Gamma}$ in Eq. (19)]. It should be cautioned that the color scales are different between the different panels.

There were three MJO events during the DYNAMO period, which are depicted in the different colors (red, green, and blue) in Fig. 10. Figure 10a is a time series of precipitation rate. The temporal transitions are depicted as the gradation of the colors. For those MJO events, the temporal transitions are also plotted in the GMS plane (Fig. 10b). This is an alternative illustration of GMS transitions to those given by Sobel et al. (2014) and Sentić et al. (2015).

The first and second MJO events shown in the reddish and greenish colors, respectively, behave consistently with the phase-plane behavior discussed in section 4c. Each convective life cycle orbits counterclockwise around the characteristic GMS line, calculated with Eq. (17), depicted as the gray line. The third MJO event in the bluish color behaves slightly differently from the first two MJO events in such a way that the slope of the orbit axis is steeper than the critical GMS. This result might imply that different MJO events have different values of the critical or the characteristic GMS, and it might be interesting to study how those are regulated.

5. Discussion

a. *Applicability of the GMS plane analysis*

The results shown in this study are based on the four simple assumptions:

1) MSE budgets are closed.
2) Column-integrated DSE anomalies are much smaller than precipitable water anomalies.
3) Precipitation is positively correlated with precipitable water.
4) The diabatic source terms can be approximated in a linear form with respect to the divergence of column DSE (or precipitation).

The second assumption does not rule out the possibility that small temperature anomalies play crucial roles in the dynamics. This second assumption is likely

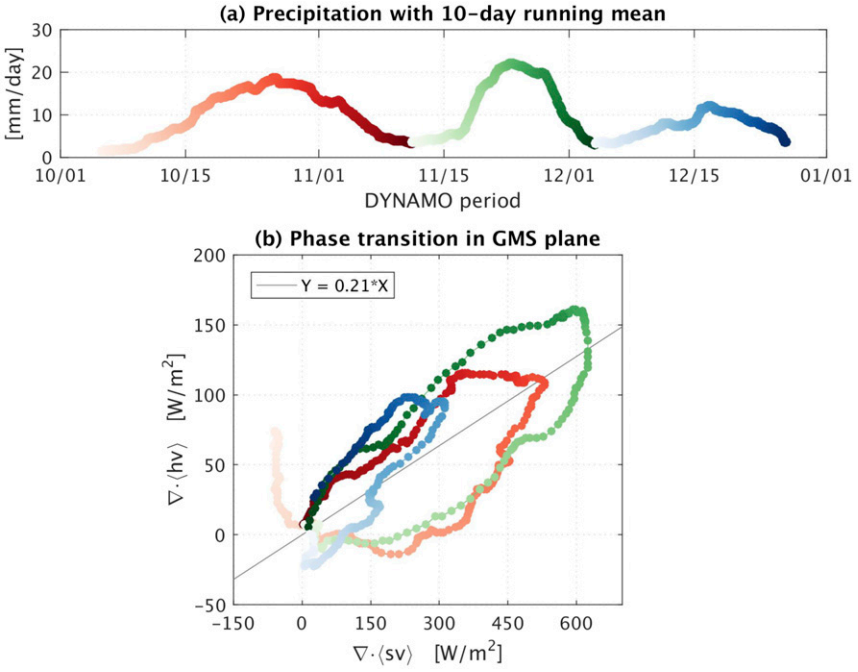

FIG. 10. (a) Time series of precipitation rate during DYNAMO. (b) Phase transitions of three MJO events shown in different colors during DYNAMO in the GMS plane. All variables are 10-day running averages. The DYNAMO field campaign was conducted from October to the end of December 2011. Plotted are data averaged over the northern sounding array.

valid only on time scales longer than a day (e.g., Inoue and Back 2015b). One would need to test the extent to which assumptions 1, 2, and 4 are valid in tropical cyclones.

As long as those assumptions are satisfied, the GMS phase transitions shown in Figs. 6 and 7 hold. The first three assumptions are generally well verified in the tropics.[4] The validity of the last assumption, which is rooted in the linear feedbacks of the cloud–radiation and the convection–evaporation, is partially less certain than the others. The cloud–radiation feedback has been well verified in the past observational studies (e.g., Lin and Mapes 2004; Inoue and Back 2015a; Johnson et al. 2015) and implemented in many theoretical models (Sobel and Gildor 2003; Fuchs and Raymond 2002; and many others). In contrast, the mechanism of the convection–evaporation feedback is not well understood, although observational studies suggested its existence (e.g., Back and Bretherton 2005). Nevertheless, both the current study and the study by Inoue and Back (2015b) with the TOGA COARE field campaign data seem to bear out the validity of the fourth assumption.

Therefore, we believe that the GMS plane analysis has a wide range of applicability, including analyses of convectively coupled equatorial waves (CCEWs) and MJO life cycles. Another benefit of this analysis is that it is applicable to all kinds of data, involving satellite, reanalysis, and field campaign data and outputs of numerical models. Thus, we expect it will provide us with a standard framework for diagnostics of tropical convective disturbances.

b. *Two aspects of GMS analysis: Time-dependent and quasi-time-independent aspects*

The GMS can be studied in two ways: as a phase transition in the GMS plane and as the characteristic GMS. The former is highly time dependent, and the latter corresponds to quasi-time-independent background GMS. This study demonstrated how to assess those different aspects separately. The transitions of time-dependent GMS can be visualized in the GMS plane as an orbiting fluctuation around the background GMS line. And the background GMS varies among different geographic locations.

These two aspects of the GMS tell us about how we should interpret the GMS in theoretical studies, which is

[4] Tropical cyclones might be the exception for the assumptions. For investigating them, the moist entropy budget could be a better choice, as demonstrated by Juračić and Raymond (2016).

given as a constant (Fuchs and Raymond 2002; Sobel and Maloney 2013; Adames and Kim 2016; and many others). To clarify that, we point out two important caveats of GMS analyses:

1) Physical interpretations of the GMS are different depending on how one computes it.
2) The characteristic GMS is the GMS associated with the moisture-mode theories.

The GMS can be calculated in various ways. For instance, we can take a ratio of spatially averaged $\nabla \cdot \langle h\mathbf{v}\rangle$ to spatially averaged $\nabla \cdot \langle s\mathbf{v}\rangle$ to get a local value of the GMS (e.g., Masunaga and L'Ecuyer 2014; Sobel et al. 2014; Inoue and Back 2015b; Sentić et al. 2015). On the other hand, we can compute the GMS from a scatterplot as in section 4d and some past studies (e.g., Raymond and Fuchs 2009; Benedict et al. 2014). In the discussion below, we demonstrate that those two versions of the GMS have distinct physical interpretations and that the GMS relevant to the moisture-mode theories is the one calculated from a scatterplot.

For proceeding with the discussion, we crudely summarize the moisture-mode theory, ignoring some details. The model of the linear moisture mode can be expressed as

$$\frac{\partial P'}{\partial t} = -(\Gamma_{\text{eff},r} + i\Gamma_{\text{eff},i}) \times P', \tag{20}$$

where P' is a precipitation anomaly, and the real component $\Gamma_{\text{eff},r}$ and the imaginary component $\Gamma_{\text{eff},i}$ are determined by the model parameters. The choice of these notations implies that they are associated with (but not equivalent to) the effective GMS.[5] The minus sign is there for consistency with the past literature.

We assume P' has the form

$$P'(x,t) = \hat{P}\exp[ikx + (\sigma_r + i\sigma_i)t], \tag{21}$$

where $\hat{P}$ is an amplitude, k is a zonal wavenumber, and σ_r and σ_i are real and imaginary frequencies, respectively. Plugging Eq. (21) into Eq. (20) yields $\sigma_r = -\Gamma_{\text{eff},r}$ and $\sigma_i = -\Gamma_{\text{eff},i}$. Thus, when $\Gamma_{\text{eff},r}$ is negative, the mode is destabilized ($\sigma_r > 0$); $\Gamma_{\text{eff},i}$ is associated with the wave propagation. In the moisture-mode models, $\Gamma_{\text{eff},r}$ is close to the effective GMS, indicating the effectively negative GMS is necessary for the destabilization of the moisture mode [see Adames and Kim (2016), which is the closest to our argument here].

The model parameters, $\Gamma_{\text{eff},r}$ and $\Gamma_{\text{eff},i}$, consist of the parameterization of four different components: horizontal MSE advection, vertical MSE advection, radiative heating, and surface fluxes. For elucidating the behavior of the GMS, let us focus on the advective term, ignoring the horizontal advection for simplicity. The argument below can be extended to include other terms.

In the context of a linear model, we can express the column-integrated vertical MSE advection as

$$\langle \omega \partial h/\partial p\rangle' = (\Gamma_{v,r} + i\Gamma_{v,i}) \times P', \tag{22}$$

where ω is vertical pressure velocity, and $\Gamma_{v,r}$ and $\Gamma_{v,i}$ are model parameters. Parameter $\Gamma_{v,r}$ contributes to the stability of the system (i.e., $\Gamma_{\text{eff},r} = \Gamma_{v,r}$ + other terms); and $\Gamma_{v,i}$ represents the contribution of the vertical MSE advection to the propagation (i.e., $\Gamma_{\text{eff},i} = \Gamma_{v,i}$ + other terms), which might be parameterized as frictionally induced moisture convergence or vertical advection by bottom-heavy ω [see Eq. (12) in Sobel and Maloney (2013) or Eq. (4a) in Adames and Kim (2016)]. The value of $\Gamma_{v,r}$, which is set to be a constant parameter, corresponds to the (vertical) GMS in the theoretical work. Now let us visualize the temporal transitions of $\langle \omega \partial h/\partial p\rangle'$ and P' expressed by Eqs. (20)–(22) as in Fig. 10.

Since this study investigated the MSE budget in Eulerian columns at fixed locations, we can set $x = 0$ in Eq. (21) without loss of generality. Because only the real component of Eq. (22) makes physical sense, plugging Eq. (21) into Eq. (22) and extracting the real component yields

$$\langle \omega \partial h/\partial p\rangle' = \hat{P}\exp(-\Gamma_{\text{eff},r}t)[\Gamma_{v,r}\cos(\Gamma_{\text{eff},i}t) + \Gamma_{v,i}\sin(\Gamma_{\text{eff},i}t)], \tag{23}$$

where we set $\sigma_r = -\Gamma_{\text{eff},r}$ and $\sigma_i = -\Gamma_{\text{eff},i}$, and we assume $\hat{P}$ is a real number. Similarly, the real components of P' and $\partial P'/\partial t$ are expressed as

$$P' = \hat{P}\exp(-\Gamma_{\text{eff},r}t)\cos(\Gamma_{\text{eff},i}t) \quad \text{and} \tag{24}$$

$$\frac{\partial P'}{\partial t} = \hat{P}\exp(-\Gamma_{\text{eff},r}t)[-\Gamma_{\text{eff},r}\cos(\Gamma_{\text{eff},i}t) - \Gamma_{\text{eff},i}\sin(\Gamma_{\text{eff},i}t)]. \tag{25}$$

Now we want to estimate the values of $\Gamma_{v,r}$ and $\Gamma_{v,i}$ from observations in order to visualize the transitions of Eqs. (23) and (24). First, in a long time series, we can approximate $\Gamma_{\text{eff},r} \simeq 0$; otherwise, the precipitation

[5] The definition of the effective GMS differs in the literature. Some authors include horizontal MSE advection in the definition (e.g., Adames and Kim 2016; Sakaeda and Roundy 2016), and others include surface evaporation in it (e.g., Hannah and Maloney 2014; Sakaeda and Roundy 2016). Here, $\Gamma_{\text{eff},r}$ is the closest to the "projected total effective GMS" in Adames and Kim (2016).

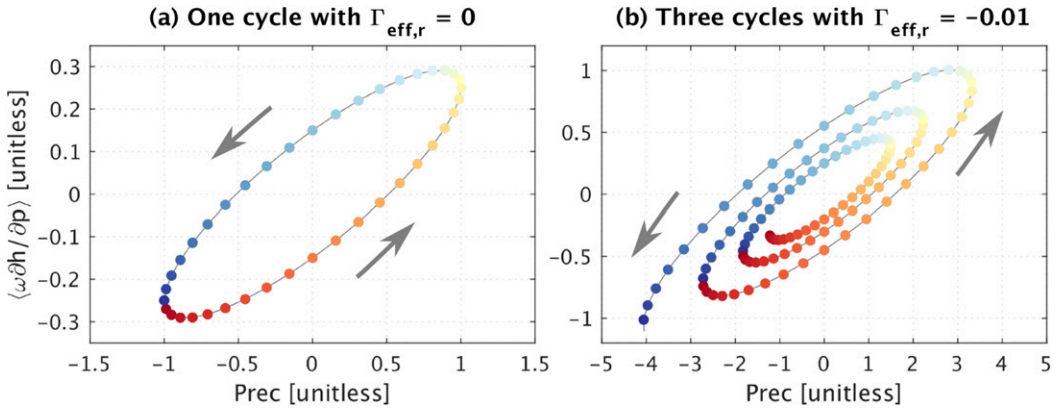

FIG. 11. (a) One cycle [the start (red dot) to the end (blue dot)] of $\langle\omega\partial h/\partial p\rangle'$ and P' expressed as Eqs. (23) and (24). For illustrative purposes, we plotted from day 20 to day 60. We set $\Gamma_{v,r} = 0.25$ and $\Gamma_{v,i} = 0.15$, with $\Gamma_{\text{eff},r} = 0$. (b) Three cycles (from day 20 to day 140) with $\Gamma_{\text{eff},r} = -0.01$.

grows infinitely or converges to zero. Therefore, we can write Eqs. (23), (24), and (25) as

$$\langle\omega\partial h/\partial p\rangle' \simeq \hat{P}[\Gamma_{v,r}\cos(\Gamma_{\text{eff},i}t) + \Gamma_{v,i}\sin(\Gamma_{\text{eff},i}t)], \tag{26}$$

$$P' \simeq \hat{P}\cos(\Gamma_{\text{eff},i}t), \quad \text{and} \tag{27}$$

$$\frac{\partial P'}{\partial t} \simeq -\hat{P}\Gamma_{\text{eff},i}\sin(\Gamma_{\text{eff},i}t). \tag{28}$$

For estimating $\Gamma_{v,r}$, we want to multiply Eq. (26) with Eq. (27) and take an integration with respect to time from 0 to 2π. In such a way, $\Gamma_{v,r}$ can be estimated in observational data as

$$\Gamma_{v,r} \simeq \frac{\overline{\langle\omega\partial h/\partial p\rangle' \times P'}}{\overline{P'^2}}, \tag{29}$$

where the bar, which represents a time average, can be considered as an integration from 0 to 2π if a time series is long enough. This is similar to the characteristic GMS defined by Eq. (17), indicating that $\Gamma_{v,r}$, which is relevant to the moisture-mode instability, can be estimated as the characteristic GMS. Similarly, we can estimate $\Gamma_{v,i}$ as

$$\Gamma_{v,i} \simeq -\Gamma_{\text{eff},i}\frac{\overline{\langle\omega\partial h/\partial p\rangle' \times \partial P'/\partial t}}{\overline{(\partial P'/\partial t)^2}}. \tag{30}$$

Similar (but not the same) methods were used by Andersen and Kuang (2012) to compute the contributions of each MSE budget term to the stabilization and to the propagation of the MJO-like variability.

For a demonstration, we set the frequency (day^{-1}) to be $\Gamma_{\text{eff},i} = 2\pi/40$. Using the TOGA COARE data (the data description is presented in the appendix), we estimated $\Gamma_{v,r}$ to be ~0.25 and $\Gamma_{v,i}$ to be ~0.05. But for illustrative purpose, we used $\Gamma_{v,i} = 0.15$ instead of 0.05. Using these values of the parameters, the temporal evolutions of Eqs. (23) and (24) are plotted in Fig. 11. Figure 11a illustrates a 40-day cycle of $\langle\omega\partial h/\partial p\rangle'$ versus P' in the neutral condition (i.e., $\Gamma_{\text{eff},r} = 0$). This neutral condition occurs when the radiative feedback and surface flux feedback effects are balanced by the GMS (or $\Gamma_{v,r}$). The cycle starts from the red dot, goes around counterclockwise, and terminates at the blue dot. This behavior is consistent with that shown in the GMS plane in Figs. 7 and 10.

This figure clarifies why the GMS is a vexing quantity. From this figure, we can calculate two distinct values of the GMS:

$$\text{GMS (background)} \sim \Gamma_{v,r} \quad \text{and} \tag{31}$$

$$\text{GMS (time–dependent)} \sim \Gamma_{v,r} + \Gamma_{v,i}\tan(\Gamma_{\text{eff},i}t), \tag{32}$$

where the former represents the slope of the major axis of the elliptic trajectory, which is calculated by Eq. (29), and the latter was computed by simply dividing Eq. (23) by Eq. (24). When we compute the GMS as a time-dependent quantity using time series, it corresponds to Eq. (32). This time-dependent GMS can easily become negative, but that negative GMS is not relevant to the stability of the moisture mode; only $\Gamma_{v,r}$ is associated with the stability.

Figures 11b illustrates the GMS plane behavior in an unstable condition where the effective GMS is set to be slightly negative ($\Gamma_{\text{eff},r} = -0.01$). This condition occurs when the radiative feedback and surface flux feedback effects exceed the background GMS. There is a growing spiral due to an exponentially amplifying oscillation, which is a characteristic of destabilized linear waves. In the real world, however, this kind of growing spiral is not expected to happen because nonlinear effects generally keep a disturbance from growing infinitely.

The distinction between the two versions of the GMS defined in Eqs. (31) and (32) becomes crucial when the size of an observational domain is smaller than that of an MJO envelope. In such a case, the contribution of the MSE advection to the propagation (i.e., nonzero $\Gamma_{v,i}$) easily makes the time-dependent GMS negative via Eq. (32). But that negative GMS must not be confused with the negative background GMS for the destabilization.

In the same sense, the drying efficiency calculated in this study is not the same as the effective GMS used in the past theoretical literature. This distinction cannot be emphasized too much because the terminology ''GMS'' is now used to mean both the time-dependent and the background ones. It is crucial to keep in mind that those two quantities must be interpreted differently: the quasi-time-independent GMS represents the stability of the background condition and thus is relevant to the moisture mode. On the other hand, the highly time-dependent GMS does not represent the background stability, but it represents ''advective drying efficiency'' via convectively induced large-scale circulations, which expresses local favorability for convection due to large-scale circulations.

6. Concluding remarks

We investigated the gross moist stability (GMS) and its related quantities utilizing satellite-based products over the tropical ocean. In the datasets used, we found the diabatic source, which is the combination of column radiation and surface fluxes, can be expressed as a linear function of the divergence of column moist static energy (MSE) with a slope of γ, which we call the critical GMS. This linear relationship, together with a positive correlation between precipitation and precipitable water, indicates that, when the GMS is less (greater) than the critical GMS, the convection amplifies (decays). This means that, if the value of the critical GMS is given, values of the GMS tell us whether the convection will amplify or decay. This statement is, however, only true when the denominator of the GMS, the divergence of column dry static energy (DSE), is positive. We generalized this condition by introducing the ''GMS plane'' analysis.

We refer to the plane of the divergence of column MSE against the divergence of column DSE as the GMS plane. In this plane, we can easily determine whether convection is in the amplifying phase or in the decaying phase. First, we draw a line going through the origin whose slope is the critical GMS. Then, if a data point lies below (above) the critical line, the convection is most likely in the amplifying (decaying) phase. Furthermore, the GMS plane behaves as a phase plane in which each convective life cycle seems like an orbiting fluctuation around the critical GMS line. We found that the GMS plane behavior is consistent even on the MJO time scale. This GMS plane behavior indicates that values of the GMS (or phase positions in the GMS plane) qualitatively predict the subsequent convective evolution. This property is theoretically important because it means we can deduce future information from the pair of the divergence of MSE and the divergence of DSE, which are both diagnostic quantities instead of prognostic quantities.

This study demonstrates that the GMS analyses have two different aspects: time-dependent and quasi-time-independent aspects. The GMS can be calculated both as a highly time-dependent quantity and as a quasi-time-independent quantity. And we can visualize those two different aspects in the GMS plane; the transitions of time-dependent GMS can be depicted in the GMS plane as an orbiting fluctuation around the quasi-time-independent GMS line. We emphasized that those two must be interpreted differently. The time-dependent GMS represents ''advective drying efficiency,'' which expresses local favorability for convection. On the other hand, the quasi-time-independent GMS represents the stability of the background condition, and it is the GMS relevant to moisture-mode theories.

We listed different calculations of the quasi-time-independent GMS: (i) a regression slope from a scatterplot and (ii) the ratio of climatological MSE divergence to climatological DSE divergence. The former GMS exhibits robust geographic patterns; the values are slightly higher in the Indian and the western Pacific Oceans than in the central–eastern Pacific and the Atlantic Oceans. The latter climatological GMS turns out to be so sensitive to data errors that we concluded that it should not be used as a diagnostic tool.

Acknowledgments. Influential conversations with Hirohiko Masunaga shaped the direction this project took. Figure 7 in this study was suggested by Christopher Bretherton. Very insightful reviews by Adam Sobel, David Raymond, and Walter Hannah significantly improved our first draft. We thank Jesse Stroik for his technical support. We also thank Tristan L'Ecuyer and William Olson for the radiative heating data, Richard Johnson and Paul Ciesielski for the DYNAMO data, and Minghua Zhang for the TOGA COARE data. The first author thanks Daniel Vimont, Gregory Tripoli, Matthew Hitchman, and Samuel Stechmann for the comments on his Ph.D. thesis, which partially contributed to this paper. This research is supported by NASA Grant NNX12AL96G and NSF Grant MSN188169.

APPENDIX

Underestimation of Characteristic GMS with Satellite Data

To check the reliability of the values of the characteristic GMSs computed with the satellite data, we compared those to the values computed with field campaign data. Two field campaign datasets were investigated: (i) the TOGA COARE field campaign data constructed by Minghua Zhang with an objective scheme called the constrained variational analysis (Zhang and Lin 1997) and (ii) the DYNAMO field campaign data used in section 4e.

Three characteristic GMSs, $\tilde{\Gamma}'$, $\tilde{\Gamma}$, and γ were computed using both the field campaign datasets and the satellite data in the same regions and were compared with each other. It should be noted that there are no overlaps of the observational time periods; the TOGA COARE and DYNAMO field campaigns were conducted, respectively, from 1 November 1992 to 28 February 1993 and from 1 October to 31 December 2011, and the satellite data used here are from 1 January 2000 to 31 December 2007. This intercomparison is implicitly dependent on the assumption that the characteristic GMSs are quasi time independent in the ITCZ.

Another important note is that the surface flux data in the TOGA COARE and DYNAMO datasets were derived in different ways. During TOGA COARE, the surface meteorology was collected from a buoy moored near the center of the domain (Weller and Anderson 1996), whereas the surface flux data during DYNAMO were obtained from TropFlux (Kumar et al. 2012), the surface meteorology of which was derived from the corrected ERA-Interim. Discussion about the differences of those datasets is beyond the scope of this study. In this study, we simply assumed the field campaign data as the ''true'' data with which the satellite estimates are compared. But it should be noted that Hannah et al. (2016) demonstrated that the field campaign sounding array is sometime inaccurate because of sparse sampling stations that provide inaccurate horizontal gradients of moisture.

The values of the characteristic GMSs are summarized in Table A1. Roughly speaking, the values of the different characteristic GMSs are consistent with each other, as claimed in section 4d. The table shows that the satellite-based ones are approximately half of those computed with the field campaign data. This result indicates that the characteristic GMSs shown in Fig. 9 might be underestimated.

However, this underestimation does not change the general conclusions presented in this study; for instance, the underestimated characteristic GMS changes the slopes in Fig. 4, but the behavior of the GMS plane discussed in section 4c is still valid. This was verified using ERA-Interim (not shown here).

It should be briefly noted that the values of the characteristic GMSs for DYNAMO are smaller than those given by Sentić et al. (2015), who used the same data as we did. This is simply because they computed the GMS with moist (dry) entropy instead of moist (dry) static energy. Generally, the GMSs computed with those different metrics exhibit different values and thus should not be compared with each other.

TABLE A1. Characteristic GMSs. The top two rows were computed with the field campaign data, and the bottom two rows were computed with the satellite data in the same regions as TOGA COARE and DYNAMO, respectively. See the text for the definition of each quantity. The value of the critical GMS for DYNAMO is slightly lower than that given in Fig. 10 because of a 10-day running average.

Data	Characteristic GMS		
	$\tilde{\Gamma}'$	$\tilde{\Gamma}$	γ
TOGA COARE (sounding)	0.257	0.263	0.217
DYNAMO (sounding)	0.171	0.195	0.187
TOGA COARE region (satellite)	0.110	0.102	0.085
DYNAMO region (satellite)	0.095	0.106	0.083

REFERENCES

Adames, Á. F., and D. Kim, 2016: The MJO as a dispersive, convectively coupled moisture wave: Theory and observations. *J. Atmos. Sci.*, **73**, 913–941, doi:10.1175/JAS-D-15-0170.1.

Andersen, J. A., and Z. Kuang, 2012: Moist static energy budget of MJO-like disturbances in the atmosphere of a zonally symmetric aquaplanet. *J. Climate*, **25**, 2782–2804, doi:10.1175/JCLI-D-11-00168.1.

Back, L. E., and C. S. Bretherton, 2005: The relationship between wind speed and precipitation in the Pacific ITCZ. *J. Climate*, **18**, 4317–4328, doi:10.1175/JCLI3519.1.

——, and ——, 2006: Geographic variability in the export of moist static energy and vertical motion profiles in the tropical Pacific. *Geophys. Res. Lett.*, **33**, L17810, doi:10.1029/2006GL026672.

——, and ——, 2009a: On the relationship between SST gradients, boundary layer winds, and convergence over the tropical oceans. *J. Climate*, **22**, 4182–4196, doi:10.1175/2009JCLI2392.1.

——, and ——, 2009b: A simple model of climatological rainfall and vertical motion patterns over the tropical oceans. *J. Climate*, **22**, 6477–6497, doi:10.1175/2009JCLI2393.1.

——, Z. R. Hansen, and Z. J. Handlos, 2017: Estimating vertical motion profile top-heaviness: Reanalysis compared to satellite-based observations and stratiform rain fraction. *J. Atmos. Sci.*, **74**, 855–864, doi:10.1175/JAS-D-16-0062.1.

Benedict, J. J., E. D. Maloney, A. H. Sobel, and D. M. W. Frierson, 2014: Gross moist stability and MJO simulation skill in three

full-physics GCMs. *J. Atmos. Sci.*, **71**, 3327–3349, doi:10.1175/JAS-D-13-0240.1.

Bretherton, C. S., and P. K. Smolarkiewicz, 1989: Gravity waves, compensating subsidence and detrainment around cumulus clouds. *J. Atmos. Sci.*, **46**, 740–759, doi:10.1175/1520-0469(1989)046<0740:GWCSAD>2.0.CO;2.

——, and A. H. Sobel, 2002: A simple model of a convectively coupled Walker circulation using the weak temperature gradient approximation. *J. Climate*, **15**, 2907–2920, doi:10.1175/1520-0442(2002)015<2907:ASMOAC>2.0.CO;2.

——, M. E. Peters, and L. E. Back, 2004: Relationships between water vapor path and precipitation over the tropical oceans. *J. Climate*, **17**, 1517–1528, doi:10.1175/1520-0442(2004)017<1517:RBWVPA>2.0.CO;2.

Charney, J. G., 1963: A note on large-scale motions in the tropics. *J. Atmos. Sci.*, **20**, 607–609, doi:10.1175/1520-0469(1963)020<0607:ANOLSM>2.0.CO;2.

Ciesielski, P. E., R. H. Johnson, K. Yoneyama, and R. K. Taft, 2014a: Mitigation of Sri Lanka island effects in Colombo sounding data and its impact on DYNAMO analyses. *J. Meteor. Soc. Japan*, **92**, 385–405, doi:10.2151/jmsj.2014-407.

——, and Coauthors, 2014b: Quality-controlled upper-air sounding dataset for DYNAMO/CINDY/AMIE: Development and corrections. *J. Atmos. Oceanic Technol.*, **31**, 741–764, doi:10.1175/JTECH-D-13-00165.1.

Curry, J. A., and Coauthors, 2004: Seaflux. *Bull. Amer. Meteor. Soc.*, **85**, 409–424, doi:10.1175/BAMS-85-3-409.

Dee, D. P., and Coauthors, 2011: The ERA-Interim reanalysis: Configuration and performance of the data assimilation system. *Quart. J. Roy. Meteor. Soc.*, **137**, 553–597, doi:10.1002/qj.828.

Fuchs, Ž., and D. J. Raymond, 2002: Large-scale modes of a nonrotating atmosphere with water vapor and cloud-radiation feedbacks. *J. Atmos. Sci.*, **59**, 1669–1679, doi:10.1175/1520-0469(2002)059<1669:LSMOAN>2.0.CO;2.

——, and ——, 2005: Large-scale modes in a rotating atmosphere with radiative-convective instability and WISHE. *J. Atmos. Sci.*, **62**, 4084–4094, doi:10.1175/JAS3582.1.

——, and ——, 2007: A simple, vertically resolved model of tropical disturbances with a humidity closure. *Tellus*, **59A**, 344–354, doi:10.1111/j.1600-0870.2007.00230.x.

Hannah, W. M., and E. D. Maloney, 2014: The moist static energy budget in NCAR CAM5 hindcasts during DYNAMO. *J. Adv. Model. Earth Syst.*, **6**, 420–440, doi:10.1002/2013MS000272.

——, B. E. Mapes, and G. S. Elsaesser, 2016: A Lagrangian view of moisture dynamics during DYNAMO. *J. Atmos. Sci.*, **73**, 1967–1985, doi:10.1175/JAS-D-15-0243.1.

Huffman, G. J., and Coauthors, 2007: The TRMM Multisatellite Precipitation Analysis (TMPA): Quasi-global, multiyear, combined-sensor precipitation estimates at fine scales. *J. Hydrometeor.*, **8**, 38–55, doi:10.1175/JHM560.1.

——, R. F. Adler, D. T. Bolvin, and E. J. Nelkin, 2010: The TRMM Multi-Satellite Precipitation Analysis (TMPA). *Satellite Rainfall Applications for Surface Hydrology*, M. Gebremichael and F. Hossain, Eds., Springer Netherlands, 3–22, doi:10.1007/978-90-481-2915-7_1.

Inoue, K., and L. Back, 2015a: Column-integrated moist static energy budget analysis on various time scales during TOGA COARE. *J. Atmos. Sci.*, **72**, 1856–1871, doi:10.1175/JAS-D-14-0249.1.

——, and L. E. Back, 2015b: Gross moist stability assessment during TOGA COARE: Various interpretations of gross moist stability. *J. Atmos. Sci.*, **72**, 4148–4166, doi:10.1175/JAS-D-15-0092.1.

Johnson, R. H., and P. E. Ciesielski, 2013: Structure and properties of Madden–Julian oscillations deduced from DYNAMO sounding arrays. *J. Atmos. Sci.*, **70**, 3157–3179, doi:10.1175/JAS-D-13-065.1.

——, ——, J. H. Ruppert, and M. Katsumata, 2015: Sounding-based thermodynamic budgets for DYNAMO. *J. Atmos. Sci.*, **72**, 598–622, doi:10.1175/JAS-D-14-0202.1.

Juračić, A., and D. J. Raymond, 2016: The effects of moist entropy and moisture budgets on tropical cyclone development. *J. Geophys. Res. Atmos.*, **121**, 9458–9473, doi:10.1002/2016JD025065.

Kumar, B. P., J. Vialard, M. Lengaigne, V. S. N. Murty, and M. J. McPhaden, 2012: TropFlux: Air–sea fluxes for the global tropical oceans—Description and evaluation. *Climate Dyn.*, **38**, 1521–1543, doi:10.1007/s00382-011-1115-0.

L'Ecuyer, T. S., and G. L. Stephens, 2003: The tropical oceanic energy budget from the TRMM perspective. Part I: Algorithm and uncertainties. *J. Climate*, **16**, 1967–1985, doi:10.1175/1520-0442(2003)016<1967:TTOEBF>2.0.CO;2.

——, and ——, 2007: The tropical atmospheric energy budget from the TRMM perspective. Part II: Evaluating GCM representations of the sensitivity of regional energy and water cycles to the 1998–99 ENSO cycle. *J. Climate*, **20**, 4548–4571, doi:10.1175/JCLI4207.1.

Lin, J.-L., and B. E. Mapes, 2004: Radiation budget of the tropical intraseasonal oscillation. *J. Atmos. Sci.*, **61**, 2050–2062, doi:10.1175/1520-0469(2004)061<2050:RBOTTI>2.0.CO;2.

Maloney, E. D., X. Jiang, S.-P. Xie, and J. J. Benedict, 2014: Process-oriented diagnosis of east Pacific warm pool intraseasonal variability. *J. Climate*, **27**, 6305–6324, doi:10.1175/JCLI-D-14-00053.1.

Masunaga, H., 2012: Short-term versus climatological relationship between precipitation and tropospheric humidity. *J. Climate*, **25**, 7983–7990, doi:10.1175/JCLI-D-12-00037.1.

——, and T. S. L'Ecuyer, 2014: A mechanism of tropical convection inferred from observed variability in the moist static energy budget. *J. Atmos. Sci.*, **71**, 3747–3766, doi:10.1175/JAS-D-14-0015.1.

Neelin, J. D., and I. M. Held, 1987: Modeling tropical convergence based on the moist static energy budget. *Mon. Wea. Rev.*, **115**, 3–12, doi:10.1175/1520-0493(1987)115<0003:MTCBOT>2.0.CO;2.

——, and J.-Y. Yu, 1994: Modes of tropical variability under convective adjustment and the Madden–Julian oscillation. Part I: Analytical theory. *J. Atmos. Sci.*, **51**, 1876–1894, doi:10.1175/1520-0469(1994)051<1876:MOTVUC>2.0.CO;2.

——, O. Peters, and K. Hales, 2009: The transition to strong convection. *J. Atmos. Sci.*, **66**, 2367–2384, doi:10.1175/2009JAS2962.1.

Peters, M. E., and C. S. Bretherton, 2005: A simplified model of the Walker circulation with an interactive ocean mixed layer and cloud-radiative feedbacks. *J. Climate*, **18**, 4216–4234, doi:10.1175/JCLI3534.1.

Raymond, D. J., 2000: Thermodynamic control of tropical rainfall. *Quart. J. Roy. Meteor. Soc.*, **126**, 889–898, doi:10.1002/qj.49712656406.

——, and Ž. Fuchs, 2007: Convectively coupled gravity and moisture modes in a simple atmospheric model. *Tellus*, **59A**, 627–640, doi:10.1111/j.1600-0870.2007.00268.x.

——, and ——, 2009: Moisture modes and the Madden–Julian oscillation. *J. Climate*, **22**, 3031–3046, doi:10.1175/2008JCLI2739.1.

——, S. L. Sessions, and Ž. Fuchs, 2007: A theory for the spinup of tropical depressions. *Quart. J. Roy. Meteor. Soc.*, **133**, 1743–1754, doi:10.1002/qj.125.

——, ——, A. H. Sobel, and Ž. Fuchs, 2009: The mechanics of gross moist stability. *J. Adv. Model. Earth Syst.*, **1**, 9, doi:10.3894/JAMES.2009.1.9.

Sakaeda, N., and P. E. Roundy, 2016: Gross moist stability and the Madden–Julian oscillation in reanalysis data. *Quart. J. Roy. Meteor. Soc.*, **142**, 2740–2757, doi:10.1002/qj.2865.

Sentić, S., S. L. Sessions, and Ž. Fuchs, 2015: Diagnosing DYNAMO convection with weak temperature gradient simulations. *J. Adv. Model. Earth Syst.*, **7**, 1849–1871, doi:10.1002/2015MS000531.

Sessions, S. L., S. Sugaya, D. J. Raymond, and A. H. Sobel, 2010: Multiple equilibria in a cloud-resolving model using the weak temperature gradient approximation. *J. Geophys. Res.*, **115**, D12110, doi:10.1029/2009JD013376.

Sobel, A. H., and C. S. Bretherton, 2000: Modeling tropical precipitation in a single column. *J. Climate*, **13**, 4378–4392, doi:10.1175/1520-0442(2000)013<4378:MTPIAS>2.0.CO;2.

——, and H. Gildor, 2003: A simple time-dependent model of SST hot spots. *J. Climate*, **16**, 3978–3992, doi:10.1175/1520-0442(2003)016<3978:ASTMOS>2.0.CO;2.

——, and J. D. Neelin, 2006: The boundary layer contribution to intertropical convergence zones in the quasi-equilibrium tropical circulation model framework. *Theor. Comput. Fluid Dyn.*, **20**, 323–350, doi:10.1007/s00162-006-0033-y.

——, and E. Maloney, 2012: An idealized semi-empirical framework for modeling the Madden–Julian oscillation. *J. Atmos. Sci.*, **69**, 1691–1705, doi:10.1175/JAS-D-11-0118.1.

——, and ——, 2013: Moisture modes and the eastward propagation of the MJO. *J. Atmos. Sci.*, **70**, 187–192, doi:10.1175/JAS-D-12-0189.1.

——, J. Nilsson, and L. M. Polvani, 2001: The weak temperature gradient approximation and balanced tropical moisture waves. *J. Atmos. Sci.*, **58**, 3650–3665, doi:10.1175/1520-0469(2001)058<3650:TWTGAA>2.0.CO;2.

——, S. Wang, and D. Kim, 2014: Moist static energy budget of the MJO during DYNAMO. *J. Atmos. Sci.*, **71**, 4276–4291, doi:10.1175/JAS-D-14-0052.1.

Su, H., and J. D. Neelin, 2002: Teleconnection mechanisms for tropical Pacific descent anomalies during El Niño. *J. Atmos. Sci.*, **59**, 2694–2712, doi:10.1175/1520-0469(2002)059<2694:TMFTPD>2.0.CO;2.

Sugiyama, M., 2009: The moisture mode in the quasi-equilibrium tropical circulation model. Part I: Analysis based on the weak temperature gradient approximation. *J. Atmos. Sci.*, **66**, 1507–1523, doi:10.1175/2008JAS2690.1.

Weller, R. A., and S. P. Anderson, 1996: Surface meteorology and air–sea fluxes in the western equatorial Pacific warm pool during the TOGA Coupled Ocean–Atmosphere Response Experiment. *J. Climate*, **9**, 1959–1990, doi:10.1175/1520-0442(1996)009<1959:SMAASF>2.0.CO;2.

Wentz, F., K. Hilburn, and D. Smith, 2012: Remote Sensing Systems DMSP SSM/I Daily Environmental Suite on 0.25 deg grid, version 7. Remote Sensing Systems, accessed 1 September 2015. [Available online at www.remss.com/missions/ssmi.]

——, T. Meissner, C. Gentemann, and M. Brewer, 2014: Remote Sensing Systems AQUA AMSR-E Daily Environmental Suite on 0.25 deg grid, version 7.0. Remote Sensing Systems, accessed 1 September 2015. [Available online at www.remss.com/missions/amsre.]

——, C. Gentemann, and K. Hilburn, 2015: Remote Sensing Systems TRMM TMI Daily Environmental Suite on 0.25 deg grid, version 7.1. Remote Sensing Systems, accessed 1 September 2015. [Available online at www.remss.com/missions/tmi.]

Yanai, M., S. Esbensen, and J.-H. Chu, 1973: Determination of bulk properties of tropical cloud clusters from large-scale heat and moisture budgets. *J. Atmos. Sci.*, **30**, 611–627, doi:10.1175/1520-0469(1973)030<0611:DOBPOT>2.0.CO;2.

Yu, J., C. Chou, and J. D. Neelin, 1998: Estimating the gross moist stability of the tropical atmosphere. *J. Atmos. Sci.*, **55**, 1354–1372, doi:10.1175/1520-0469(1998)055<1354:ETGMSO>2.0.CO;2.

Zhang, M. H., and J. L. Lin, 1997: Constrained variational analysis of sounding data based on column-integrated budgets of mass, heat, moisture, and momentum: Approach and application to ARM measurements. *J. Atmos. Sci.*, **54**, 1503–1524, doi:10.1175/1520-0469(1997)054<1503:CVAOSD>2.0.CO;2.